Available online at www.sciencedirect.com
SCIENCE DIRECT
Geochimica et Cosmochimica Acta 70 (2006) 608–621
Geochimica
www.elsevier.com/locate/gca

Dissolution of jarosite [$KFe_3(SO_4)_2(OH)_6$] at pH 2 and 8: Insights from batch experiments and computational modelling

Adrian M.L. Smith [a,b,c,1], Karen A. Hudson-Edwards [a,*], William E. Dubbin [b], Kate Wright [c,2]

[a] Research School of Earth Sciences at UCL-Birkbeck, Birkbeck, University of London, Malet Street, London, WC1E 7HX, UK
[b] Department of Mineralogy, The Natural History Museum, Cromwell Road, London, SW7 5BD, UK
[c] Davy Faraday Research Laboratory, The Royal Institution of Great Britain, 21 Albemarle Street, London, W1S 4BS, UK

Received 26 January 2005; accepted in revised form 26 September 2005

Abstract

Jarosite [$KFe_3(SO_4)_2(OH)_6$] is a mineral that is common in acidic, sulphate-rich environments, such as acid sulphate soils derived from pyrite-bearing sediments, weathering zones of sulphide ore deposits and acid mine or acid rock drainage (ARD/AMD) sites. The structure of jarosite is based on linear tetrahedral–octahedral–tetrahedral (T–O–T) sheets, made up from slightly distorted FeO_6 octahedra and SO_4 tetrahedra. Batch dissolution experiments carried out on synthetic jarosite at pH 2, to mimic environments affected by ARD/AMD, and at pH 8, to simulate ARD/AMD environments recently remediated with slaked lime ($Ca(OH)_2$), suggest first order dissolution kinetics. Both dissolution reactions are incongruent, as revealed by non-ideal dissolution of the parent solids and, in the case of the pH 8 dissolution, because a secondary goethite precipitate forms on the surface of the dissolving jarosite grains. The pH 2 dissolution yields only aqueous K, Fe, and SO_4. Aqueous, residual solid, and computational modelling of the jarosite structure and surfaces using the GULP and MARVIN codes, respectively, show for the first time that there is selective dissolution of the A- and T-sites, which contain K and SO_4, respectively, relative to Fe, which is located deep within the T–O–T jarosite structure. These results have implications for the chemistry of ARD/AMD waters, and for understanding reaction pathways of ARD/AMD mineral dissolution.

1. Introduction

Jarosite [$KFe_3(SO_4)_2(OH)_6$] occurs commonly in the oxidised portions of sulphide ore deposits (Dutrizac and Jambor, 2000), fluvial environments contaminated by acid rock or acid mine drainage (ARD, AMD) (Hudson-Edwards et al., 1999), wastes produced from the metallurgical extractive industry (Arregui et al., 1979; Dutrizac and Jambor, 2000), acid sulphate soils (Schwertmann, 1961; Dudas, 1984; Hyashi, 1994) and clay seams and beds (Alpers et al., 1992; Dutrizac and Jambor, 2000). Jarosite is of considerable geological, environmental, and metallurgical interest because it sorbs and co-precipitates considerable amounts of potentially toxic elements such as As and Pb (Dutrizac, 1983; Bigham and Nordstrom, 2000).

Jarosite is a member of the isostructural jarosite-alunite group of minerals that has a general formula of $AB_3(TO_4)_2(OH)_6$, where A represents cations with a coordination number $\geqslant 9$, and B and T represent cation sites with octahedral (O) and tetrahedral (T) coordination, respectively (Jambor, 1999; Hawthorne et al., 2000). In ideal jarosite [$KFe_3(SO_4)_2(OH)_6$], the B site cation is Fe(III), the A site is occupied by a cation (mainly K^+, but also H_3O^+, hydronium; Brophy and Sheridan, 1965; Kubisz,

* Corresponding author. Fax: +44 207 679 2867.
E-mail address: k.hudson-edwards@geology.bbk.ac.uk (K.A. Hudson-Edwards).
[1] Present address: Entec UK Ltd, Canon Court North, Abbey Lawn, Abbey Foregate, Shrewsbury, SY2 5DE, UK.
[2] Present address: Centre for Sustainable Resource Processing, Nanochemistry Research Institute, Department of Applied Chemistry, Curtin University of Technology, G.P.O. Box U1987, Perth, WA 6845, Australia.

0016-7037/$ - see front matter © 2005 Elsevier Inc. All rights reserved.
doi:10.1016/j.gca.2005.09.024

1970; Dutrizac and Kaiman, 1976; Ripmeester et al., 1986) in 12-fold coordination, and the T site is filled by sulphate (SO_4^{2-}) (Kubisz, 1964; Brophy and Sheridan, 1965). The jarosite structure contains Fe vacancies, and 'additional water' in the form of hydronium (Kubisz, 1970; Härtig et al., 1984; Ripmeester et al., 1986; Alpers et al., 1989), and the chemical formula is therefore more correctly written as $H_3O_{1-x}\ K_xFe_{3-y}\ [(OH)_{6-3y}(H_2O)_{3y}\ (SO_4)_2]$.

Jarosite typically forms in ferric-rich, acidic (pH < 3), oxic environments, and readily breaks down when removed from its stability region by presumably converting to iron(III) oxide or oxyhydroxide phases (Stoffregen and Rye, 1992; Stoffregen et al., 2000). It has been proposed that jarosite converts to goethite through the following reaction

$$KFe_3(SO_4)_2(OH)_{6(s)} \leftrightarrow 3FeO(OH)_{(Goethite)} + K^+_{(aq)} + 2SO^{2-}_{4(aq)} + 3H^+_{(aq)} \quad (1)$$

but the mechanisms of this reaction, and the specific products formed, have not been studied in detail. This knowledge is critical in modelling and predicting geochemical reactions in metallurgical and, particularly, natural AMD/ARD environments. Furthermore, elucidating the fate of K, SO_4^{2-}, and Fe during jarosite dissolution will aid the development of robust models that describe the geochemical cycling of these elements in AMD/ARD systems. However, much of the work on jarosite dissolution has been conducted at temperatures of 40–400 °C (e.g., Dutrizac and Jambor, 2000), even though AMD/ARD environments are much lower temperature (generally <25 °C). Some dissolution studies at ⩽25 °C have been carried out, but these have not characterised the reaction product solids in detail (e.g., Baron and Palmer, 1996; Gasharova et al., 2005). Therefore, the objectives of this study were to: (1) monitor the breakdown and release of constituent elements (K, Fe, and SO_4) from synthetic jarosite using dissolution batch experiments and, (2) characterise new phase(s) formed as a result of jarosite dissolution. Because jarosite dissolution is ultimately related to its structure, a third objective was to computationally model the jarosite structure as a means to provide atomic level insights into dissolution mechanisms.

2. Methods and materials

2.1. Experimental studies

2.1.1. Synthesis of jarosite

Jarosite was synthesised following the method of Baron and Palmer (1996). Briefly, a 100 mL solution of 1.0 M KOH (BDH, Aristar grade) and 0.351 M $Fe_2(SO_4)_3{\cdot}5H_2O$ (Aldrich) was heated to 95 °C with constant stirring at 400 rpm in a covered 400 mL beaker at 1 atm. After 4 h reaction, the precipitate was allowed to settle and the supernatant solution decanted. The precipitate was then washed several times with ultrapure water (18 MΩ cm^{-1}) then dried at 110 °C for 24 h.

2.1.2. Characterisation of synthetic jarosite

The precipitation products were identified as jarosite using powder X-ray diffraction (XRD) analysis with a Philips PW1050 vertical powder diffractometer utilising Co Kα radiation at 35 kV and 30 mA at 25 °C. Unit cell parameters were calculated through Rietveld refinement. Refinement of the lattice parameters was carried out using GSAS (Larson and Von Dreele, 1998) and the 'model free' Le Bail Method (Le Bail et al., 1988) where individual '$|F_{obs}|$' are obtained by Rietveld decomposition from arbitrarily identical values. In addition to the structure factors, free refinement was made of the lattice parameters constrained according to the rhombohedral symmetry of the space group in the centred hexagonal setting, background, profile parameters, and the instrumental zero-point. In all cases, a pseudo-voigt profile was used (Larson and Von Dreele, 1998).

For quantitative total elemental analysis, approximately 60 mg of synthetic jarosite was dissolved in a polypropylene beaker by adding concentrated HCl dropwise until no solid remained. The solutions were then diluted to 50 mL with 2% HNO_3 and analysed for K, Fe, and S by inductively coupled plasma optical emission spectrometry (ICP-OES) on a Varian Vista-Pro (axial configuration) using a simultaneous solid-state detector (CCD). All analytical ICP-OES results were within one standard deviation of the mean.

Fourier transform infrared spectroscopy (FTIR) was used to characterize the vibrational modes within the synthetic jarosite. Spectra were collected with a Perkin-Elmer Spectrum One FTIR Spectrometer using the KBr pellet (Ø13 mm) technique (McMillan and Hofmeister, 1988). The spectra (400–4000 cm^{-1}) were recorded in transmission mode immediately after pellet preparation. Five scans were accumulated, each with a resolution of 4 cm^{-1}.

Particle morphology of the jarosite was determined using a Philips XL30 FEG scanning electron microscope (SEM) operating at 5.0 kV and with a spot size of 3.0. Surface area was determined by nitrogen multipoint BET analysis with a Micromeritics Gemini III 2375 surface area analyser.

2.1.3. Dissolution experiments

Both acidic dissolution batch experiments, which mimic environments affected by ARD/AMD, and alkaline dissolution batch experiments, which mimic ARD/AMD environments recently remediated with slaked lime ($Ca(OH)_2$), were carried out following the procedure of Baron and Palmer (1996). Briefly, for both sets of experiments, 100 mg of oven-dry synthetic jarosite were added to 500 mL of ultrapure water (18 MΩ cm^{-1}). For the acid dissolution, the initial pH was set to 2.0 by the dropwise addition, while stirring, of concentrated $HClO_4$. For the alkali dissolution, the initial pH was adjusted to 8.0 in a similar fashion, with the addition of 0.01 M $Ca(OH)_2$ (BDH, AnalaR grade). Both the acid and alkaline dissolutions, conducted in triplicate at 20 °C and 1 atm, were

unbuffered, thus allowing free drift of pH. All pH measurements were obtained with an Accument AP50 meter equipped with a Russel Emerald pH electrode. The jarosite suspensions were transferred to 750 mL acid washed Amber HDPE bottles, then agitated gently with a Stuart SRT2 Roller Mixer operating at a fixed speed of 33 rpm.

Ten mL aliquots of each suspension were obtained periodically by pipette while an overhead stirrer (~50 rpm) maintained a uniform suspension. All aliquots were filtered through 0.025 μm MF Millipore filters. A 4.5 mL sub-sample of the filtered suspension was then acidified to yield a 1% v/v HNO_3 matrix, which was subsequently analysed for Fe_{tot}, K_{tot}, and S_{tot}. All S was assumed to be present as SO_4^{2-}. The pH of each bulk solution was measured during each sampling episode. At the end of each dissolution experiment, the residual jarosite and any associated solid was recovered by filtration through a 0.22 μm MF Millipore filter, allowed to air dry at 20 °C in a desiccator, then stored in an air-tight plastic vial.

The pH and concentrations of K_{tot}, Fe_{tot}, and $SO_{4\,tot}$ at steady state were used to calculate equilibrium aqueous activities of K^+, Fe^{3+}, and SO_4^{2-} with The Geochemist's Workbench (GWB) version 4.0.2 (Bethke, 1996). Activity coefficients and saturation indices were calculated using the extended form of the Debye–Hückel equation described by Helgeson (1969) and the latest form of the GWB thermodynamic database (based on the 1996 revision of the EQ3/6 database; Wolery, 1979, 1996 and data from Baron and Palmer, 1996). Eh versus pH diagrams were constructed in GWB using the measured equilibrium activities from bottle 2 of the acid dissolution experiments, and bottle 1 of the alkali dissolution experiments.

The residual solids were identified by powder XRD analysis at 25 °C using a Siemens D500 diffractometer operating at 40 kV and 40 mA and equipped with a scintillation counter. Cu Kα radiation ($\lambda = 1.54056$ Å) was selected with a secondary graphite monochromator. The residual solids were characterised further using quantitative wet chemical analysis, SEM and FTIR, as previously described for the synthetic jarosite.

2.2. Computational modelling

Classical atomistic simulation methods, based on the Born model, use interatomic potential functions to describe the forces acting between atoms or ions in a solid. In ionic materials, these forces are dominated by long range Coulombic or electrostatic interactions, but also include contributions from short-range repulsive interactions due to overlap of nearest neighbour electron clouds. Such short-range forces acting between non-bonded ions are well described by the Buckingham potential

$$U_{ij}^{\mathrm{Buck}} = A_{ij}\exp-\left(r_{ij}/\rho_{ij}\right) - C_{ij}r_{ij}^{-6}, \tag{2}$$

where A_{ij} and ρ_{ij} describe the repulsion between two ions i and j at a separation r, and C_{ij} is included to model dispersion. For bonded interactions such as those within molecules, we use a Morse potential of the form

$$U_{ij}^{\mathrm{Morse}} = D\left(1 - \mathrm{e}^{-\alpha(r_{ij}-r_0)}\right)^2 - 1, \tag{3}$$

where D corresponds to the dissociation energy of the bond, r_0 is the equilibrium bond length and α is related to the vibrational frequency of the stretching mode. To model the directionality of O–S–O bonds we use the harmonic three-body potential of the form

$$U_{(\theta ijk)} = \tfrac{1}{2}k_{ijk}(\theta - \theta_0)^2, \tag{4}$$

where k_{ijk} is the bond-bending force constant between the ions i, j, and k and θ_0 is the reference tetrahedral angle.

The variable potential parameters are derived by fitting to experimental data such as structure, elastic constants and vibrational spectra. Simulations are then carried out using standard energy minimization schemes in which the energy of the system is calculated with respect to all atomic coordinates and thus the equilibrium positions of the ions are evaluated by minimising the lattice energy until all forces acting on the crystal are removed.

The variable parameters for the Buckingham interactions used in this study were initially taken from standard potential models (Woodley et al., 1999) developed for the component oxides, and combined with Morse potentials for the sulphate (Allan et al., 1993) and the hydroxyl ions (Saul et al., 1985). Although the structure obtained in this way was acceptable, the Buckingham terms used to link the different parameters were modified so as to better reproduce the experimental data. The GULP code (Gale, 1997) was used to perform a least squares fit to the structure of jarosite as measured by Menchetti and Sabelli (1976), and the full set of parameters used is presented in Table 1.

To simulate the structure of surfaces, the crystal is treated as planes of atoms that are periodic in two-dimensions. Surfaces are modelled by considering a simulation block that is divided into two regions. The first region, R1, is composed of those atoms that are adjacent to the surface, while those below, in R2, represent the bulk crystal. All atoms in region R1 are allowed to relax to their minimum energy configurations, while those in R2 are kept fixed at their bulk equilibrium positions. All bulk calculations reported in this study were performed with GULP1.3 (Gale, 1997), while surfaces were modelled using the MARVIN code (Gay and Rohl, 1995).

3. Results

3.1. Characterisation of synthetic jarosite

The combination of KOH and $Fe_2(SO_4)_3{\cdot}5H_2O$ produced a yellow precipitate of Munsell colour 10YR 8/7. The precipitate was identified as endmember potassium jarosite by comparing its powder X-ray diffraction pattern with that reported in the International Centre for Diffrac-

Table 1
Potential parameters for the model of the jarosite structure

	A (eV)	ρ (Å)	C (eV Å^6)	Reference
Two-body short range interaction				
Buckingham				
K^+–$O1^{0.84-}$	987.570	0.3000	0.00	[a]
K^+–$O3^{1.426-}$	1587.570	0.3000	0.00	[a]
Fe^{3+}–$O1^{0.84-}$	3219.335	0.2641	0.00	[b]
Fe^{3+}–$O3^{1.426-}$	3219.335	0.2641	0.00	[b]
$O1^{0.84-}$–$O1^{0.84-}$	103585.02	0.2000	25.98	[c]
$O1^{0.84-}$–$O3^{1.426-}$	103585.02	0.2000	25.98	[c]
$O3^{1.426-}$–$O3^{1.426-}$	103585.02	0.2000	25.98	[c]
	D_e (eV)	β (Å^{-1})	r_0 (Å)	
Morse				
$S^{1.36+}$–$O1^{0.84-}$	5.0000	1.2000	1.4650	[a]
$O3^{1.426-}$–$H^{0.426+}$	7.0525	2.1986	0.9685	[d]
	k_3 (eV rad^{-2})	θ (°)		
Three-body interaction				
$O1^{0.84-}$–$S^{1.36+}$–$O1^{0.84-}$	15.0	109.47		[c]

The short range potential cut-off was set to 10 Å.
[a] Fitted from Allan et al. (1993).
[b] Fitted from Lewis and Catlow (1985).
[c] Allan et al. (1993).
[d] Saul et al. (1985).

tion Data Powder Diffraction Files (ICDD PDF 22-0827). All the peaks produced by the precipitate related to the structure of jarosite; the absence of extraneous peaks indicated that no other phases were present at detectable levels (Fig. 1A). The calculated lattice parameters of the synthetic jarosite are $a_0 = 7.3137(6)$ and $c_0 = 17.0730(5)$, in contrast to the standard ICDD PDF file values ($a_0 = 7.29$; $c_0 = 17.13$).

Atomic percentages of the A-, B-, and T-site elements were determined using the wet chemical data. The molecular composition of the synthetic jarosite, calculated using the modified formula of Kubisz (1970), is $(H_3O)_{0.16}K_{0.84}Fe_{2.46}(SO_4)_2(OH)_{4.38}(H_2O)_{1.62}$, which is comparable to other studies (e.g., Baron and Palmer, 1996), except for the low Fe occupation at the B-site (i.e., 2.46 in this study, compared to an ideal of 3.00). The large number of Fe vacancies can explain the lower than expected *c*-axis value for the synthetic jarosite, and supports the hypothesis of structural defects in the A- and B-sites proposed by Kubisz (1970).

The FTIR spectra for the synthetic jarosite (Fig. 2A) are similar to those previously reported (Powers et al., 1975; Serna et al., 1986; Baron and Palmer, 1996; Sasaki et al., 1998; Drouet and Navrotsky, 2003). The intense absorption observed in the region 2900–3700 cm^{-1} can be attributed to O–H stretching (ν_{OH}). Three hydroxyl groups surround each of the sulphate oxygen atoms, which are located on trigonal axes, parallel to the *c*-axis of the unit cell (Hendricks, 1937). Hendricks (1937) suggested that the hydrogen atoms were orientated in such a way as to bind to these oxygen atoms, thus forming OH–OSO_3 hydrogen bonds. Drouet and Navrotsky (2003) found that there was a direct correlation between lower O–H stretching frequencies and decreases in the *c*-axis parameter across the K–Na jarosite solid solution, where the *a*-axis parameter remained nearly constant. A-site cations are thought to have little influence on a_o and are theoretically responsible for the main variations in c_o (Jambor and Dutrizac, 1983). It is possible to distinguish two vibrational modes around the hydrogen atom: O–H and H–OSO_3. The band observed at 1634–1641 cm^{-1} (Fig. 2A) is attributed to HOH deformation, in agreement with the results of others (Powers et al., 1975; Baron and Palmer, 1996; Drouet and Navrotsky, 2003). The HOH deformation mode is directly related to the 'additional' water groups formed from the protonation of the hydroxyl groups.

The jarosite shows irregular and globular form (Fig. 3), with various grain sizes, although the majority are 1–5 μm, and the smallest 0.1 μm. Some of the grains show cleaved sides that may be signs of mechanical abrasion arising from stirring during the synthesis. Similar particle morphologies for synthetic jarosite are reported elsewhere (Bigham, 1994; Baron and Palmer, 1996; Dutrizac and Jambor, 2000; Sasaki and Konno, 2000). The surface area of the synthetic jarosite is 1.4 m^2 g^{-1}, considerably lower than the 4.0 m^2 g^{-1} obtained by Sasaki and Konno (2000). However, these authors synthesised the jarosite using a procedure that differs from ours.

3.2. Dissolution experiments

3.2.1. Dissolution at pH 2

3.2.1.1. Solution chemistry. Most of the dissolution at pH 2 occurred within the first 500 h, with rates declining rapidly

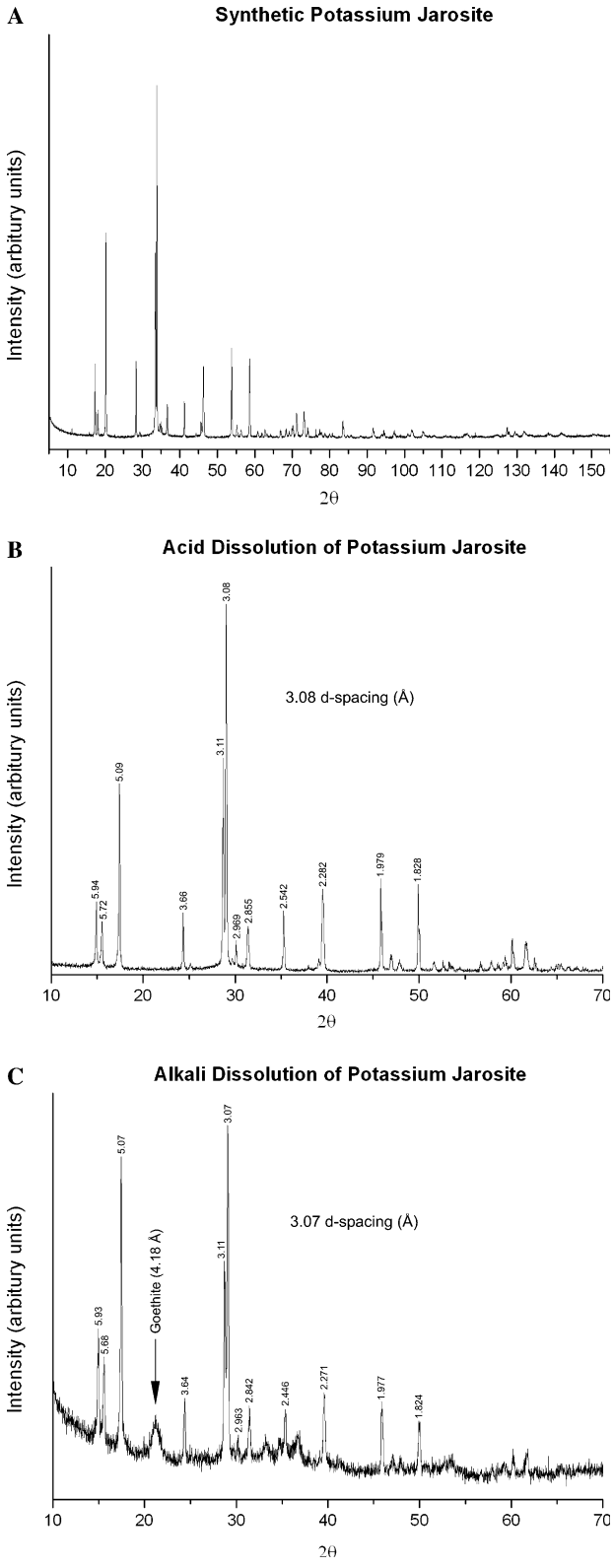

Fig. 1. Powder X-ray diffraction patterns of (A) the original synthetic jarosite, (B) residual solids from the acidic (pH 2) dissolution, and (C) residual solids from the alkaline (pH 8) dissolution. Samples were mounted on a Bruker zero background silicon (510) sample holder and analysed using Cu Kα radiation ($\lambda = 1.54056$ Å), 2-θ range 10–70°, step size 0.020° and step time 27 s. d-spacings have been indicated for the strongest peaks.

with time and steady-state conditions achieved at approximately 3000 h, which is comparable to other studies (Fig. 4A; Table 2). The final K concentration was between 0.2088 and 0.2044 mmol L^{-1} (Table 2), and the pH remained nearly constant over the duration of the experiment ($pH_{initial} = 2.0$; $pH_{final} = 2.02 - 2.03$). Molar ratios of K^+, Fe^{3+}, and SO_4^{2-} in solution were calculated with respect to SO_4^{2-}, which is assigned a value of 2, a convention frequently used in calculating the molecular composition of jarosite (Baron and Palmer, 1996). The K molar ratio in solution varied from 1.24 to 1.25 and the Fe ratio varied from 2.34 to 2.36.

Calculated equilibrium aqueous activities and saturation indices (calculated for steady-state conditions and using the K_{sp} from Baron and Palmer, 1996, which is incorporated in the Geochemist's Workbench database) for the dissolution at pH 2 are compiled in Tables 3 and 4, respectively. The charge balance error among the three replicates ranged from 3 to 6% (Table 3). Saturation indices for hematite and goethite were positive, while that for jarosite was negative (Table 4).

3.2.1.2. Residual solids. Total element concentrations, and their molar ratios, in residual solids from each of the three replicates are summarised in Table 5. Once again SO_4^{2-} is assigned, by convention, a molar ratio of 2. The K molar ratio in the residual solids varied from 0.669 to 0.673 while that for the Fe ranged from 2.652 to 2.692.

The XRD patterns and FTIR spectra for the acidic dissolution solids were both similar to those for the unaltered synthetic jarosite (compare Figs. 1A, B and 2A, B), with no extra peaks (XRD) or bands (FTIR) relating to additional phases present. The residual solid was lighter and more uniform in colour than the original synthetic jarosite, with the former possessing a yellower hue and a higher chroma (Munsell colour 2.5Y 8/8). The majority of the post-dissolution jarosite grains have a degree of surface roughness and show extensive and deep pitting (Fig. 5). Neither micrograph in Fig. 5 shows any evidence of a new phase, consistent with the XRD and FTIR data.

3.2.2. Dissolution at pH 8

3.2.2.1. Solution composition. In the alkali dissolution experiment the majority of the dissolution occurred within the first 1500 h, with rates declining with time (Fig. 4B). The pH decreased from an initial value of 8.0 to a value of 3.26–3.30 at the termination of the reaction. The dissolved Fe concentration remained near detection limit throughout the experiment in all three replicates; at the end of the reaction the dissolved Fe varied from 0.0023 to 0.0025 mmol L^{-1}. Steady-state was judged to have occurred after approximately 3500–4000 h, based on the solution profiles for replicates 2 and 3. The final total concentrations of K, Fe, and SO_4 at steady state, and their corresponding molar ratios, are presented in Table 2. Molar ratios of K^+ and Fe^{3+} in solution were once again calculated

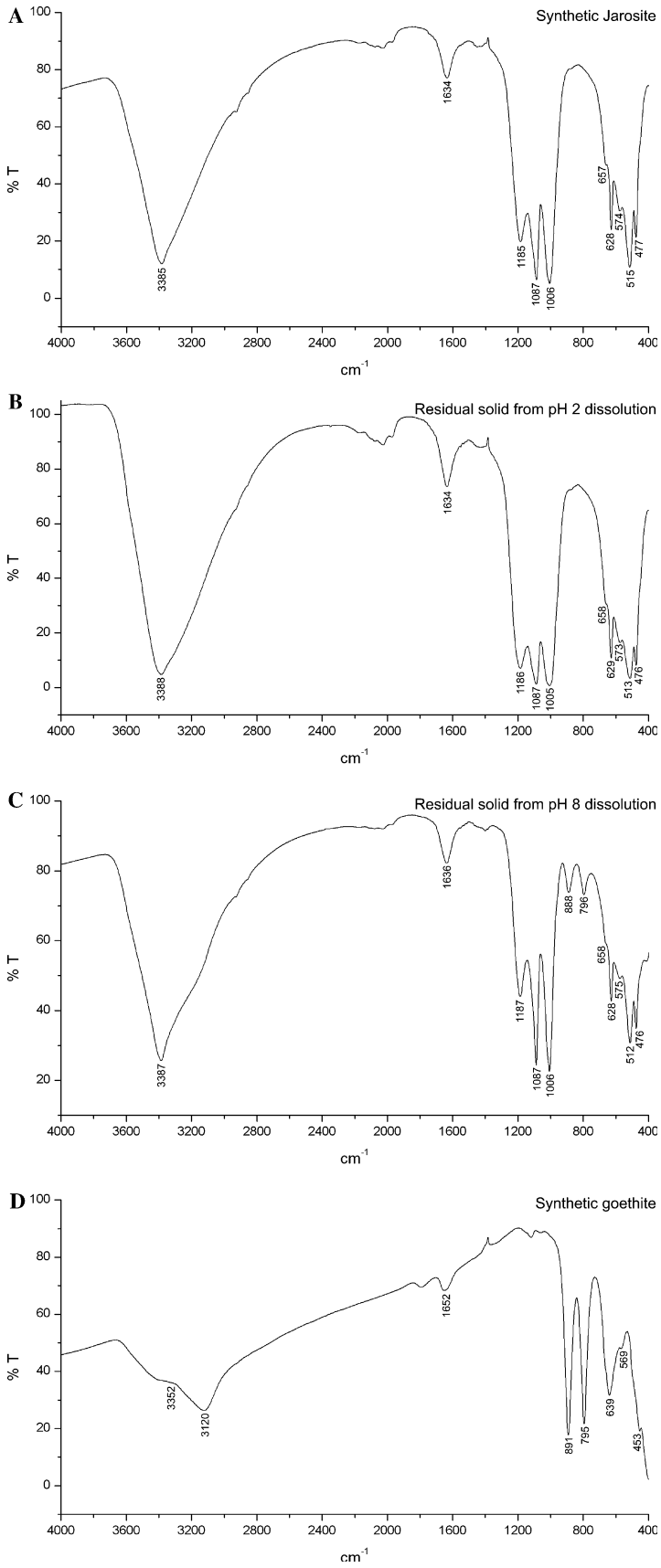

Fig. 2. Fourier transform infrared spectra (FTIR) of (A) the synthetic jarosite, (B) residual solids from the acidic (pH 2) dissolution, (C) residual solids from the alkaline (pH 8) dissolution, and (D) synthetic goethite. The range was 400–4000 cm^{-1} with a resolution of 4 cm^{-1}, five scans were accumulated. The main vibrational bands in the spectrum are marked.

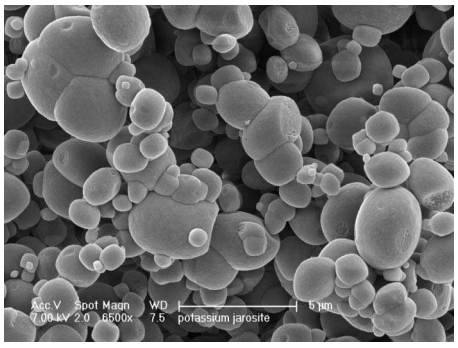

Fig. 3. Scanning electron microscope (SEM) image of synthetic jarosite. Operating conditions are indicated on the photomicrograph.

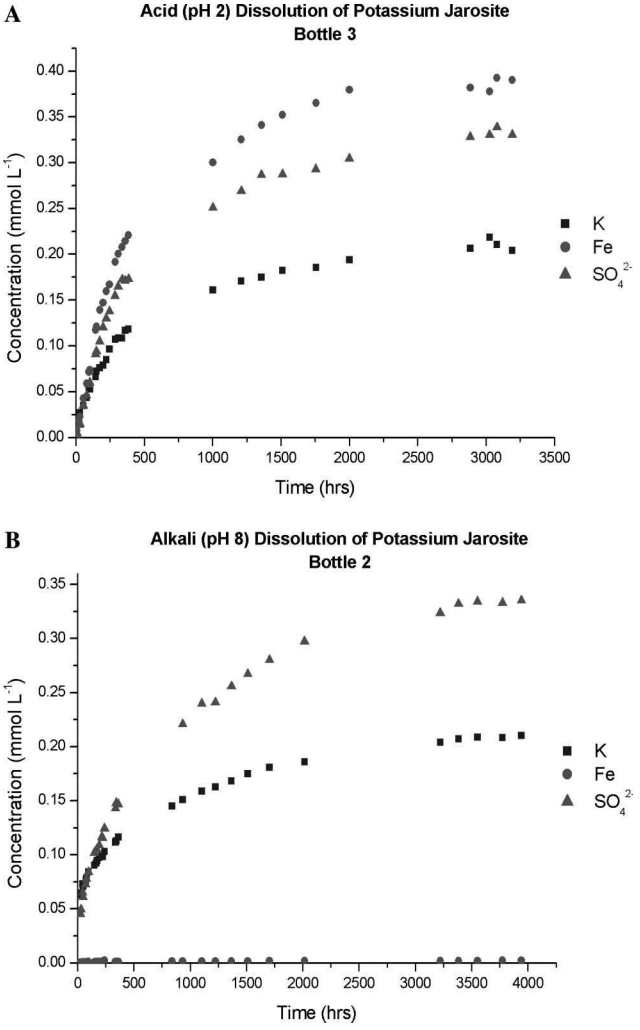

Fig. 4. Concentrations of K_{tot}, Fe_{tot}, and $SO_{4\,tot}$ in solution for (A) bottle 3 of the acid (pH 2) dissolution, and (B) bottle 2 of the alkali (pH 8) dissolution of jarosite, plotted against time.

assuming that SO_4^{2-} has a stoichiometric value of 2. The K molar ratio in solution varied from 1.24 to 1.26 and the Fe ratio from 0.0136 to 0.0149.

Equilibrium aqueous activities for the jarosite dissolution are presented in Table 3. The charge balance error among the three replicates ranged from 7 to 8%. Considering only those minerals with log Q/K greater than −3, positive saturation indices were found for hematite and goethite, whilst those for jarosite and $Fe(OH)_3$ were negative (Table 4).

3.2.2.2. Residual solids. Concentrations and molar ratios of K, Fe, and SO_4^{2-} in the solids remaining after dissolution at pH 8 are summarised in Table 5. The K molar ratio in the residual solids varied from 0.672 to 0.681, and the Fe ratio from 4.799 to 4.853. XRD analyses show that the principal constituent is jarosite (Figs. 1A and C). An additional broad peak at approximately 21° 2θ is attributed to goethite (ICDD PDF 03-0249), its width suggesting this phase possesses both poor crystallinity and small particle size.

An FTIR spectrum of the solids recovered following the alkali dissolution experiments is shown in Fig. 2C. Although this spectrum is broadly similar to that of the unaltered jarosite (Fig. 2A), two additional bands at 888 and 796 cm^{-1} are present. These bands are positively identified as O–Fe vibrations arising from the crystal structure of goethite [α-FeO(OH)]. For comparison, Fig. 2D shows an FTIR spectrum of synthetic goethite, which yields these distinctive O–Fe vibrations at 891 and 795 cm^{-1}.

The residual solid has a Munsell colour of 7.5YR 5.5/8, indicating a redder hue as compared to the original synthetic jarosite. Bigham (1994) reported that goethite found in ARD ochres possesses hues varying from 7.5YR to 10YR.

Fig. 6 shows particle morphology of the residual solid following the pH 8 dissolution. A dominant feature of the residuum is the 'frost-like' coatings on the grain surfaces. The grains also show varying degrees of pitting, but generally to a much lesser extent than that seen in the acid dissolution (Fig. 5). At higher magnification (Fig. 6B), one can see the needle or rod-like morphology of a secondary phase coating the smooth globular surfaces. The needle shaped crystallites vary in size, from approximately 10 to 100 nm (Fig. 6). The external morphology of this secondary phase is similar to the short rod-like form of goethite described previously (Bigham, 1994). Precipitation of goethite as a result of the dissolution of jarosite has also been suggested by Gasharova et al. (2005) in a recent AFM study.

3.3. Computational modelling of the jarosite structure

3.3.1. Bulk structure

The structure of jarosite is based on linear tetrahedral–octahedral–tetrahedral (T–O–T) sheets, made up from slightly distorted BO_6 octahedrons and TO_4 tetrahedrons. Each octahedron has four bridging hydroxyl groups in a plane, and sulphate oxygen atoms at the apices. Three of the tetrahedral oxygen atoms are coordinated to metals ions (B), and the symmetry of the TO_4^{2-} tetrahedra is reduced from T_d to C_{3v}. The metal ions are joined by these TO_4^{2-} tetrahedra and by the network of di-hydroxyl bridges

Table 2
Final pH and aqueous concentrations (mmol L^{-1}) and molar ratios for the dissolution experiments

Compound	Final pH	Concentrations			Molar ratios		
		K	Fe	SO_4	K	Fe	SO_4
pH 2 dissolutions	2.02–2.03	0.2044–0.2088	0.3900–0.3904	0.3304–0.3332	1.24–1.25	2.34–2.36	2
pH 8 dissolutions	3.26–3.30	0.2041–0.2123	0.0023–0.0025	0.3279–0.3383	1.24–1.26	0.0136–0.0149	2

Table 3
Calculated equilibrium activities

Compound	pH	Log activity			Charge balance error (%)	Calculated log IAP
		log $\{SO_4^{2-}\}$	log $\{K^+\}$	Log $\{Fe^{3+}\}$		
pH 2 dissolution	2.02–2.04	−3.90 to −3.96	−3.67 to −3.74	−3.96 to 4.02	3–6	-11.30 ± 0.25 to -11.38 ± 0.25
pH 8 dissolution	3.26–3.30	−3.55–3.57	−3.69 to −3.71	−6.97 to −7.03	7–8	

Table 4
Calculated saturation indices

Compound	Saturation indices (log Q/K)[a]
pH 2 dissolution	hematite 4.07–4.13 goethite 1.55–1.58 jarosite −1.99 to (−1.88)
pH 8 dissolution	hematite 5.50–5.61 goethite 2.27–2.32 jarosite −2.81 to (−2.70) $Fe(OH)_3$ −2.85 to (−2.80)

[a] Only minerals with log $Q/K > -3$ are listed.

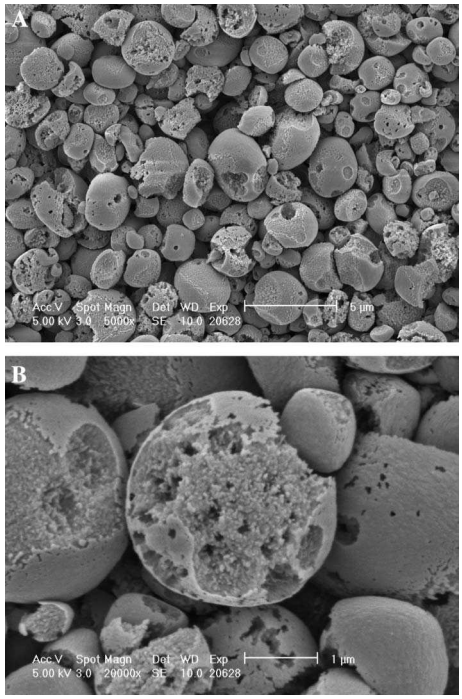

Fig. 5. SEM images of the residual solid from the acid (pH 2) dissolution of jarosite.

to form sheets separated by the uncoordinated sulphate oxygen atom and the alkali A-site cations (Jambor, 1999; Becker and Gasharova, 2001). The key relationships in the jarosite structure are illustrated in Fig. 7. There are three crystallographically distinct oxygen sites (Fig. 7B), where O1 and O2 are part of the SO_4^{2-} group, and O3 is a hydroxyl oxygen. Within our model, O1 and O2 are equivalent and have a charge of −0.84, while O3 has a charge of −1.426.

The simulated structural parameters of jarosite are given in Table 6, along with the experimentally determined values for comparison. The computationally modelled crystallographic axes are within 2% of those determined experimentally (Menchetti and Sabelli, 1976) and maintain the correct a/c ratio. All bond lengths and angles are also in good agreement. Ideally, we would like to compare measured physical data such as elastic constants with those calculated by our model, but no other experimental data are available against which the model could be tested.

3.3.2. Surface structure

Experimental SEM and AFM morphology studies of synthetic jarosite show that the crystals are predominantly terminated by the most stable {012} faces (Becker and Gasharova, 2001; Gasharova et al., 2005). Triangular (001) faces are seen, but most disappear in favour of the {012} faces in larger crystals (Becker and Gasharova, 2001). The (001) surfaces, when cleaved, lead to the formation of a surface which is charged and therefore the simulation block will have a net dipole. In the notation of Tasker

Table 5
Residual solid concentrations (mmol L^{-1}) and molar ratios for the dissolution experiments

Compound	Concentrations			Molar ratios		
	K	Fe	SO_4	K	Fe	SO_4
pH 2 dissolutions	0.1552–0.1582	0.6147–0.6345	0.4636–0.4713	0.669–0.673	2.652–2.692	2
pH 8 dissolutions	0.1221–0.1265	0.8745–0.8943	0.3614–0.3713	0.672–0.681	4.799–4.853	2

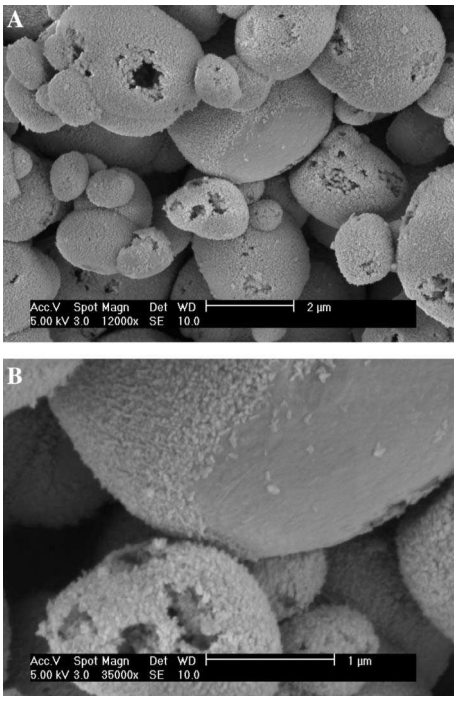

Fig. 6. Scanning electron micrograph (SEM) images of the residual solid from the alkali dissolution of jarosite. Image (A) is a general overview of the residual solid showing a fine crystalline coating. Image (B) is a high-resolution micrograph showing a few jarosite grains; a fine needle-like crystalline coating is evident. Operating conditions are indicated on each micrograph.

(Tasker, 1979) this is a type III surface. For such a surface, the magnitude of the dipole, and hence the calculated surface energy, will depend on the depth of the simulation block. In nature, this type of surface will neutralise the dipole by reconstruction of the ions in the surface layer, by hydroxylation or by some other interaction with ions around it. The {0 1 2} surface, however, can be cleaved in such a way as to produce two different, but non-charged surfaces. The investigation of the jarosite surfaces was therefore limited to these two terminations in the {0 1 2} planes.

The two surfaces, which are designated S1 and S2, were created using the MARVIN code and modelled under simulated vacuum conditions at absolute zero. Region I and region II were 10 and 26 Å thick, respectively. S1 comprises neutral sub-layers of composition $[KFe(OH)_4]^0$ as illustrated in Fig. 8A, which shows the atomic arrangement and the accessible surface contour. The accessible surface is that which would be obtained by running a probe of 1 Å radius across the surface. On relaxation, the undercoordinated Fe^{3+} octahedron rotates and distorts, causing half of the OH groups adjacent to the surface to rotate such that they move above the plane of the surface. The other surface OH groups also move, though to a much lesser degree. The Fe^{3+} ions sink down into the bulk while the K^+ ions move upwards. There is also a slight distortion and rotation of the SO_4 groups as they move down into the bulk.

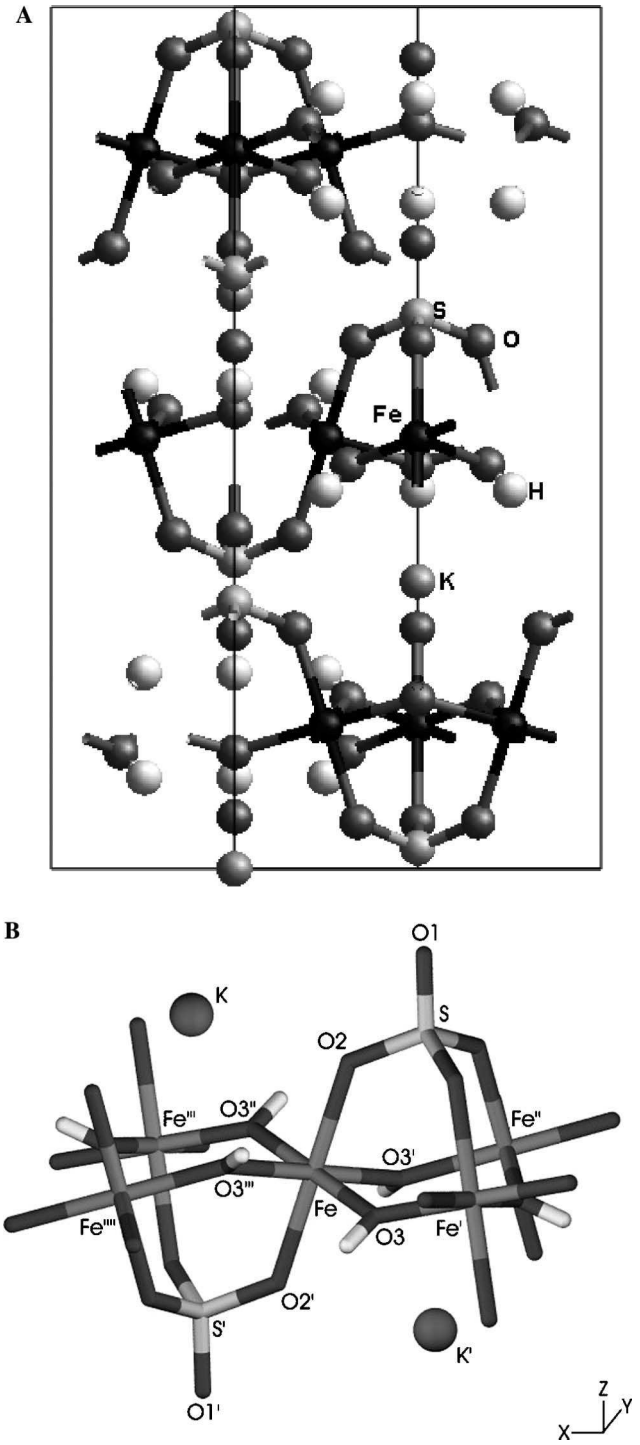

Fig. 7. (A) *X–Z* axes cut through a rigid ion potential model of jarosite. The structure is composed of FeO_6 octahedra bonded to sulphate tetrahedra, making a tetrahedral–octahedral–tetrahedral (T–O–T) sheet-like structure. Potassium ions are located in 12-fold coordination between the T–O–T sheets. (B) High-resolution schematic diagram of the key T–O–T building blocks and the 12-fold coordinated A-site in the potassium jarosite structure. Specific atomistic structural positions are labelled with respect to the central Fe atom.

The net effect of these relaxations is to open up the surface (Fig. 8B), facilitating the removal of K^+ and to a lesser extent, SO_4^{2-}, during dissolution. The accessible

Table 6
Structural and experimental parameters of jarosite

	Experimental			Calculated		
a, *b*	7.315			7.443		
c	17.224			17.497		
K	0.00000	0.00000	0.00000	0.00000	0.00000	0.00000
S	0.00000	0.00000	0.30880	0.00000	0.00000	0.31719
Fe	0.00000	0.50000	0.50000	0.00000	0.50000	0.50000
O1	0.00000	0.00000	0.39360	0.00000	0.00000	0.40096
O2	0.22340	−0.22340	−0.05450	0.22181	0.77819	0.95187
O3	0.12680	−0.12680	0.13570	0.12474	0.87526	0.14073
H	0.16900	−0.16900	0.10600	0.18668	0.81332	0.11932

Experimental parameters are from Menchetti and Sabelli (1976).

surface area of the simulation cell increases from 205 to 254 $Å^2$ on relaxation. S2, which comprises neutral sub-layers with compositions $[Fe_2(SO_4)_2(OH)_2]^0$, behaves quite differently, and only experiences minimal relaxation. There is a slight rotation of the SO_4 tetrahedra inwards towards the bulk, which has the effect of closing off the surface, reducing its accessible area slightly from 191 to 187 $Å^2$. The relative stability of the two surfaces can be determined by comparing their surface energies, defined as the work done to cleave the surface from the bulk crystal. For our two surfaces, the initial unrelaxed energies are the same (1.67 Jm^{-2}) while the relaxed energies are 0.89 and 1.19 Jm^{-2} for surface 1 and 2, respectively. These energies are for a crystal cleaved under vacuum and may well change for a simulation carried in the presence of a solvent.

4. Discussion

4.1. Dissolution at pH 2 and 8

The K, Fe, and SO_4 concentration profiles for both the pH 2 and 8 experiments (Fig. 4) display characteristics of parabolic rate kinetics: a rapid initial release of constituent ions to solution, followed by an ever-decreasing rate of dissolution. Where the solution concentration for each constituent ion was constant, the dissolution reaction had reached quasi-steady state. The profiles also suggest that

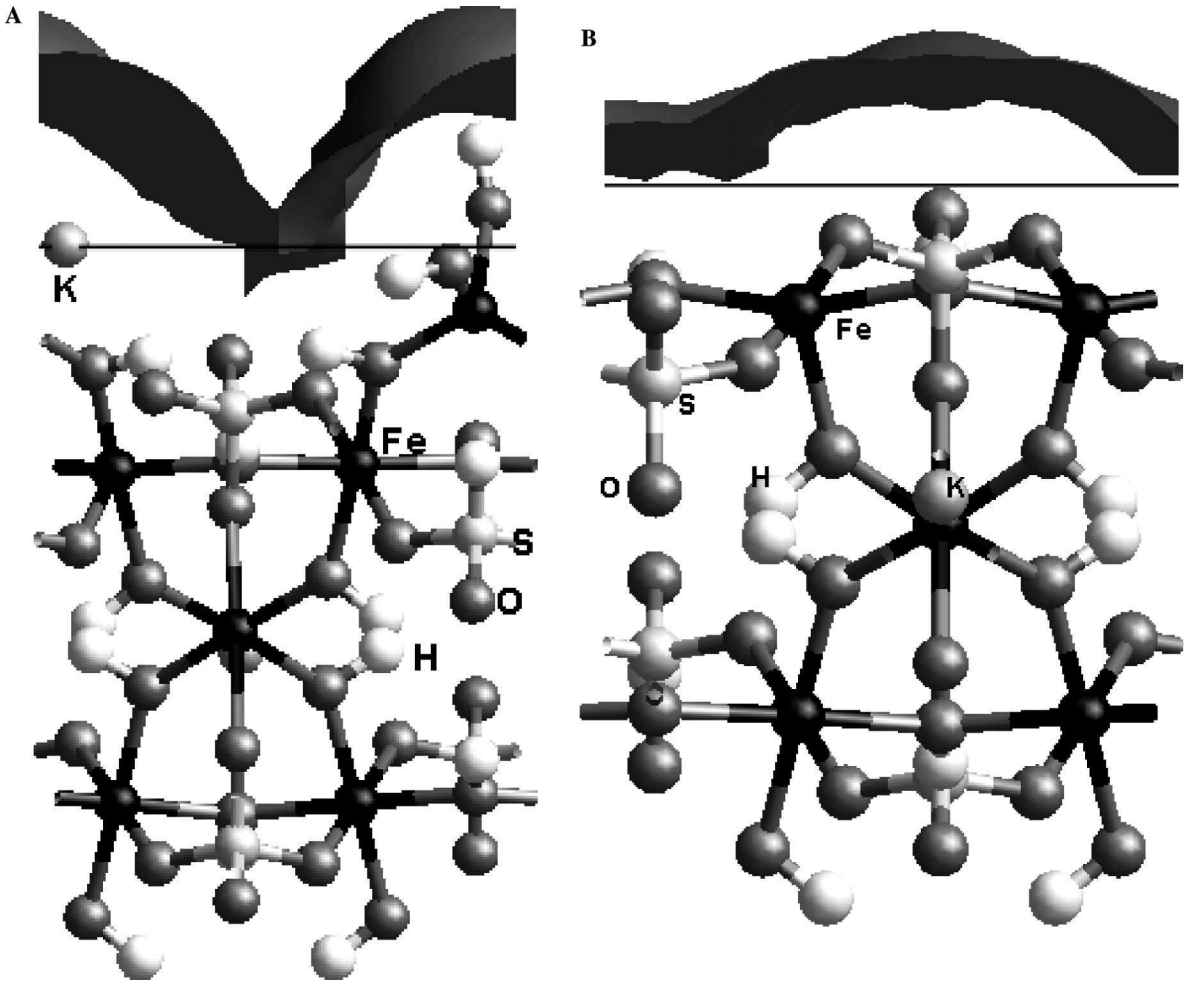

Fig. 8. *X*–*Z* axis cuts of the face 1 termination of {0 1 2} group of faces of jarosite. The surface comprises neutral sub-layers with compositions $[KFe(OH)_4]^0$. Before relaxation (A) the surface is terminated by O3 oxygens of the hydroxyl group and K ions in the A-site. Face 1 experiences a degree of rotation of the T–O–T during surface relaxation (B). The resulting rotation upon relaxation in face 1 is terminated by K ions and the hydrogen ions of the hydroxyl group.

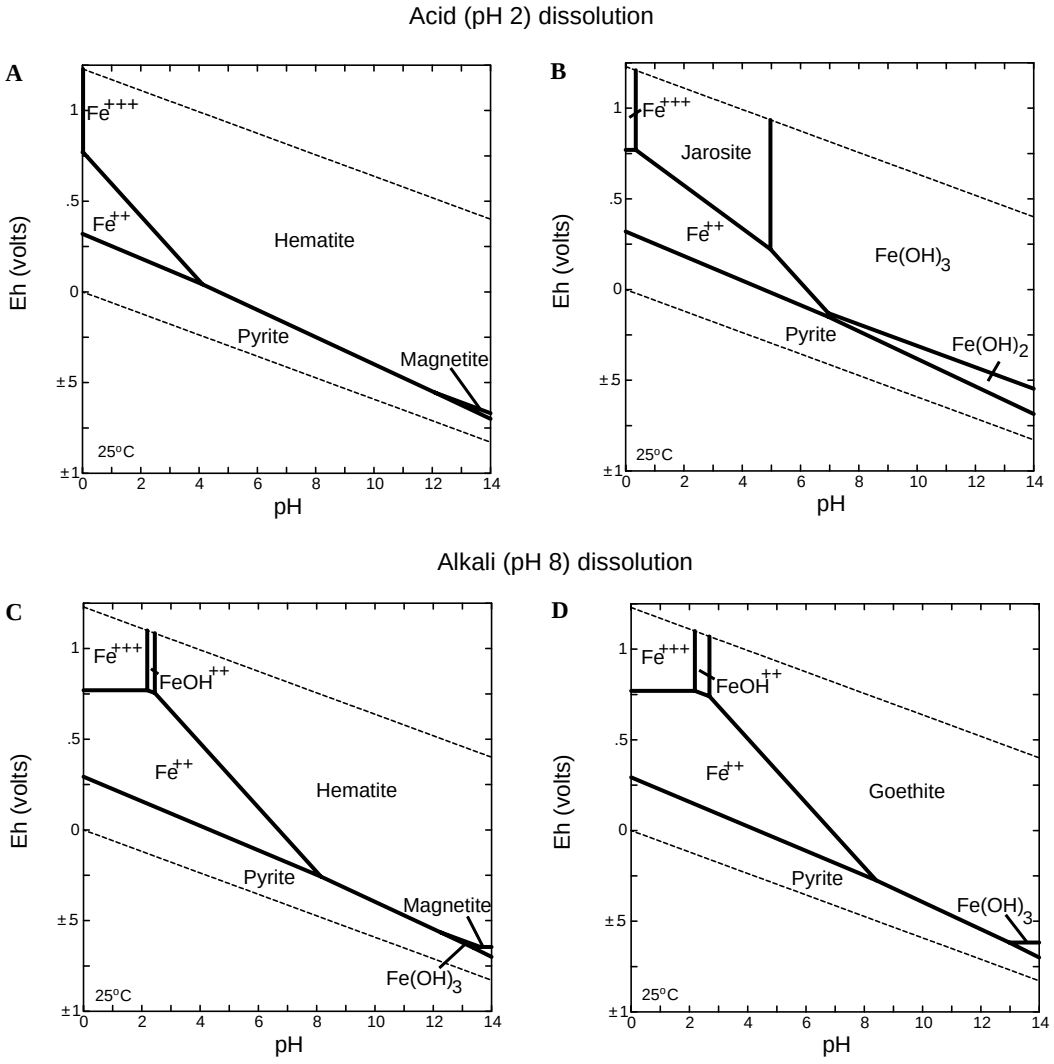

Fig. 9. Eh-pH diagrams for the acid (pH 2; A and B) and the alkali (pH 8; C and D) dissolutions of jarosite. Equilibrium aqueous activities were taken from bottle 2 for the pH 2 dissolution, and from bottle 1 for the alkali dissolution. (A and C) are Eh-pH diagrams in which all possible minerals are shown, and (B and D) are Eh-pH diagrams in which hematite and a series of other minerals (FeO, magnetite, pyrrhotite, and troilite) have been suppressed to simulate the experimental conditions.

a transport-controlled dissolution model (cf., Stumm and Morgan, 1996) governed these particular dissolution experiments, although this cannot be proved without further investigations into the effects of temperature, stirring rate and the secondary goethite phase in the pH 8 experiments.

A comparison of the K, Fe, and SO_4 molar ratios for the aqueous solution and residual solid following dissolution at pH 2, with those of the calculated formula of the synthetic jarosite, reveals some interesting relationships. The molar ratios of aqueous K and SO_4 (i.e., 1.24–1.25 and 2, Table 2) indicate that there is excess dissolved K relative to SO_4, when compared with the calculated K:SO_4 ratio of 0.84:2 for the original jarosite (this difference, and the others discussed below are significant at $\alpha = 0.005$). There is a deficiency of K in the solid relative to SO_4 (i.e., 0.669–0.673:2; Table 5). Similar deviation from ideality is observed for Fe and SO_4, though in this case Fe is deficient in solution relative to SO_4, as shown by the aqueous Fe:SO_4 molar ratio of 2.34–2.36:2 (Table 2) (compare with the ideal Fe:SO_4 molar ratio of 2.46:2 in the original jarosite). The residual solid molar ratio data are consistent with the observed Fe deficiency in solution, as indicated by a higher than ideal Fe:SO_4 ratio in the residual solid (i.e., 2.652–2.692:2 versus 2.46:2; Table 5). These data provide empirical evidence consistent with our model predictions described previously in this paper. Specifically, distortion of the jarosite surface as illustrated in Fig. 8 facilitates preferential dissolution of K and, to a lesser extent, SO_4, while Fe, which is sterically remote, remains the least labile of the ions. Such close agreement between experiment and model predictions of K, Fe, and SO_4 release from jarosite, to our knowledge the first reported in the literature, serves to validate our model and lends support to the use of atomistic simulation methods more broadly for the prediction of jarosite dissolution in aqueous environments.

All three ions, K^+, Fe^{3+}, and SO_4^{2-}, show varying degrees of incongruency with respect to their concentrations in solution at steady state. For this reason, the dissolution

of jarosite at pH 2 is incongruent, with the reaction as follows:

$$KFe_3(SO_4)_2(OH)_{6(s)} + H^+_{(aq)} \rightarrow xK^+_{(aq)} + yFe^{3+}_{(aq)} + zSO^{2-}_{4(aq)} \quad (5)$$

Dissolution at pH 8 is also incongruent, as shown by the non-ideal dissolution of the parent ions K and SO_4 (Tables 2 and 5) and the formation of an Fe-rich secondary phase (i.e., goethite) (Figs. 1 and 2). The reaction for this dissolution is

$$KFe_3(SO_4)_2(OH)_{6(s)} + OH^-_{(aq)} \rightarrow xFeO(OH)_{(s)} + yK^+_{(aq)} + zSO^{2-}_{4(aq)} \quad (6)$$

The calculation of the IAP for the dissolution of a mineral is important, because at equilibrium, the IAP is equal to the solubility product, K_{SP}. If the dissolution of jarosite is re-written as in Eq. 7, then the IAP for these two reactions would be as in Eq. 8:

$$KFe_3(SO_4)_2(OH)_{6(s)} + 6H^+_{(aq)} \rightarrow K^+_{(aq)} + 3Fe^{3+}_{(aq)} + 2SO^{2-}_{4(aq)} + 6H_2O_{(l)} \quad (7)$$

$$\log IAP = \log\{K^+\} + 3\log\{Fe^{3+}\} + 2\log\{SO_4^{2-}\} + 6\log\{H_2O\} + 6pH \quad (8)$$

Calculation of IAP values and solubility products requires that equilibrium be reached. This can be facilitated through the use of excess solid, as in our study, to ensure that sufficient jarosite remains at equilibrium. Incongruent dissolution and the precipitation of secondary solids, while not precluding the calculation of IAP and K_{SP}, complicate their derivation considerably. This study has shown that both the acidic and alkaline dissolution of jarosite are incongruent. We urge caution, therefore, when using published IAP and K_{SP} values for modelling jarosite dissolution. The incongruency of the dissolution also calls into question the positions for the contours of stability relations in an $\log a^2_{H^+} a_{SO_4^{2-}}$ versus $\log a^2_{K^+} a_{SO_4^{2-}}$ diagram determined by Stoffregen (1993) for jarosite, hematite, and Fe(SO$_4$)(OH). The contours were based on an assumption that a version of the reaction shown in Eq. (5), above, described congruent dissolution.

Speciation modelling and calculated saturation indices predict the stability of hematite and goethite in the experimental system (Table 4). Hematite is commonly reported as a positive saturation index in nearly all aqueous, Fe^{3+}-rich oxic environments by programs like GWB, reflecting its stability and widespread occurrence in many natural environments. The slight positive index for goethite (1.55–1.58) indicates that, over a long period, goethite may precipitate during the pH 2 dissolution of jarosite. The saturation index for goethite in the pH 8 experiment is higher than that for the pH 2 experiment, and is corroborated by the formation of this mineral as a product of the pH 8 dissolution. Figs. 9A and C show Eh-pH stability fields in which all possible minerals were considered. For both dissolution experiments, hematite is the dominant solid, although its field is larger in the pH 2 dissolution. When hematite and a series of other minerals (FeO, magnetite, pyrrhotite, and troilite) are removed from the model, an Eh-pH diagram that is more representative of the experimental conditions is produced (Figs. 9B and D). In the pH 2 diagram (Fig. 9B), jarosite is a stable phase between pH 0.5 and 5, as predicted by Baron and Palmer (1996), and the other stable phase is $Fe(OH)_3$. In the pH 8 diagram, by contrast, goethite is the most stable phase, and jarosite is unstable (Fig. 9D).

4.2. Environmental implications

Both the experimental data and computational modelling show that the dissolution of jarosite is incongruent. Selective dissolution of the A- and T-sites, which contain K and SO_4, respectively, results in higher concentrations of these ions in solution relative to Fe, which is located deep within the T–O–T structure in the original solid. Becker and Gasharova (2001) have reported similar selective dissolution of K and SO_4 on a jarosite surface. This incongruency may explain the high aqueous concentrations of SO_4 and, to a lesser extent, K, in many AMD/ARD systems (e.g., Hudson-Edwards et al., 1999). In these systems, although some of the K and SO_4 released could be sorbed onto phases such as illite, or precipitated as gypsum or other soluble sulphate salts, a considerable proportion could remain in solution if the reactions are not favourable. Our data suggest that these K or SO_4 do not resorb onto secondary phases such as goethite (Table 2). Therefore, sulphate arising from jarosite dissolution may contribute to unacceptably high levels of this anion, which, in many AMD/ARD environments, exceed the international limit of 250 mg/L for SO_4 in potable water (WHO, 1996, 1998).

This study has shown that goethite forms as a secondary phase when jarosite dissolves in alkaline environments, a phenomenon that has been predicted previously (e.g., Stoffregen and Rye, 1992; Nordstrom and Munoz, 1994; Dutrizac and Jambor, 2000; Stoffregen et al., 2000), and observed in the field (e.g., Bigham, 1994). Although we found no evidence for the formation of metastable schwertmannite or ferrihydrite during the dissolution, as observed by others (e.g., Bigham and Nordstrom, 2000), we sampled the residual solid only after several hundred hours had passed, and thus may have characterised only the stable end-product. The goethite that we characterised may comprise the original, or slightly re-arranged, FeO_6 octahedra that remain after the preferential dissolution of the K and SO_4 ions. The low but detectable amounts of aqueous Fe in the dissolution experiments (Table 2) suggest that the goethite may instead have formed by precipitation of aqueous species. The extremely low solubility of $Fe^{3+}_{(aq)}$ in oxic environments ($<10^{-18}$ M at pH 6; Schwertmann, 1991) will favour such precipitation (Fig. 9D). More precisely, the Fe ions may be involved in a dynamic dissolution–precipitation cycle (viz., Putnis, 2002), in which they are hydroxyl-

ated, move away from the surface, react with other Fe–O–OH complexes (that are exposed because of the loss of SO_4 and K ions) then reprecipitate as goethite.

In the acidic dissolution experiments, approximately 25–30% of the original solid dissolved, while in the alkali dissolutions only 15–20% of the original solid dissolved. The reduced dissolution under alkali conditions can be attributed to the precipitation on the jarosite surface of secondary phases that evidently acted as partial inhibitors of dissolution. All of the dissolution reactions were of a batch reactor design and, more importantly, were closed systems. The natural environment, however, is an open system, in which pH, temperature, and solution composition can change quickly and markedly. The results of our study could be verified and refined by repeating the experiments using a flow-through reactor system that more closely approximates natural ARD/AMD environments. As indicated by Dutrizac and Jambor (2000), it is likely that precipitation of the aqueous Fe^{3+} will displace the jarosite dissolution equilibrium and cause more jarosite to dissolve, resulting in the conversion of all jarosite to goethite.

5. Conclusions

The dissolution of jarosite at both pH 2 and 8 is incongruent, with selective dissolution of K and SO_4 compared to Fe. We have shown for the first time that this incongruency is related to the high stability of the FeO_6 octahedra, with Fe located deep within the T–O–T jarosite structure, and the lower stability of the $[KFe(OH)_4]^0$ {012} surface relative to the $[Fe_2(SO_4)_2(OH)_2]^0$ {012} surface. While the pH 2 dissolution yields only aqueous products, the pH 8 experiments result in formation of nanoparticles of secondary goethite on the jarosite grain surfaces, which do not resorb either K or SO_4. These surface coatings are probably responsible for inhibiting subsequent jarosite dissolution. All of these results help to explain the cycling of SO_4 and, to a lesser extent, K in ARD/AMD waters, and confirm the importance of goethite in these environments.

Acknowledgments

This work was funded through a UK Engineering and Physical Sciences Research Council (EPSRC) studentship award (number 309778) to A.M.L. Smith. We thank A.S. Wills for the GSAS refinement of the original synthetic jarosite, J. Wilson for assistance with thermodynamic modelling, C. Jones and A. Ball for help with SEM analysis and photography, G. Jones and V. Din for assistance with geochemical analysis, and I. Wood, G. Cressey and C. Kirk for expert help with the XRD analysis. The authors thank two anonymous reviewers and associate editor Carrick Eggleston for their insightful comments.

Associate editor: Carrick M. Eggleston

References

Allan, N.L., Rohl, A.L., Gay, D.H., Catlow, C.R.A., Davey, R.J., Mackrodt, W.C., 1993. Calculated bulk and surface properties of sulfates. *Faraday Disc.* **95**, 273–280.

Alpers, C.N., Rye, R.O., Nordstrom, D.K., Ball, J.W., 1989. Solubility of jarosite solid solutions precipitated from acid mine waters, Iron Mountain, California, U.S.A.. *Sci. Géol. Bull.* **42**, 281–298.

Alpers, C.N., Rye, R.O., Nordstrom, D.K., White, L.D., King, Bi-Shia, 1992. Chemical, crystallographic and stable isotopic properties of alunite and jarosite from acid-hypersaline Australian lakes. *Chem. Geol.* **96**, 203–226.

Arregui, V., Gordon, A.R., Steintveit, G., 1979. The jarosite process: past, present and future. In: Cigan, J.M., Mackey, T.S., O'Keefe, T. (Eds.), *Lead-Zinc-Tin'80*. The Mineralogical Society of AIME, Warrendale, PA, pp. 97–123.

Baron, D., Palmer, C.D., 1996. Solubility of jarosite at 4–35 °C. *Geochim. Cosmochim. Acta* **60**, 185–195.

Becker, U., Gasharova, B., 2001. AFM observations and simulations of jarosite growth at the molecular scale: probing the basis for the incorporation of foreign ions into jarosite as a storage mineral. *Phys. Chem. Miner.* **28**, 545–556.

Bethke, C.M., 1996. *Geochemical Reaction Modelling*. Oxford University Press, New York.

Bigham, J.M., 1994. Mineralogy of ochre deposits formed by sulphide oxidation. In: Jambor, J.L., Blowes, D.W. (Eds.), *The Environmental Geochemistry of Sulfide Mine-Wastes*, vol. 22. Mineralogical Association of Canada Short Course, pp. 103–132.

Bigham, J.M., Nordstrom, D.K., 2000. Iron and aluminium hydroxysulfates from acid sulphate waters. In: Alpers, C.N., Jambor, J.L., Nordstrom, D.K. (Eds), *Sulfate Minerals: Crystallography, Geochemistry, and Environmental Significance*. Reviews in Mineralogy and Geochemistry 40. pp. 351–403.

Brophy, G.P., Sheridan, M.F., 1965. Sulfate studies IV: the jarosite–natrojarosite–hydronium jarosite solid solution series. *Am. Miner.* **50**, 1595–1607.

Drouet, C., Navrotsky, A., 2003. Synthesis, characterization, and thermochemistry of K–Na–H_3O jarosites. *Geochim. Cosmochim. Acta* **67**, 2063–2076.

Dudas, M.J., 1984. Enriched levels of arsenic in post-active acid sulphate soils in Alberta. *Soil Sci. Soc. Am. J.* **48**, 1451–1452.

Dutrizac, J.E., 1983. Factors affecting alkali jarosite precipitation. *Metall. Trans. B* **14B**, 531–539.

Dutrizac, J.E., Jambor, J.L., 2000. Jarosites and their applications in hydrometallurgy. In: Alpers, C.N., Jambor, J.L., Nordstrom, D.K. (Eds.), *Sulfate Minerals: Crystallography, Geochemistry, and Environmental Significance*. Reviews in Mineralogy and Geochemistry 40, pp. 405–452.

Dutrizac, J.E., Kaiman, S., 1976. Synthesis and properties of jarosite-type compounds. *Can. Miner.* **14**, 151–158.

Gale, J.D., 1997. GULP: a computer program for the symmetry-adapted simulation of solids. *J. Chem. Soc. Faraday Trans.* **93**, 629–637.

Gasharova, B., Göttlicher, J., Becker, U., 2005. Dissolution at the surface of jarosite: an in situ AFM study. *Chem. Geol.* **215**, 499–516.

Gay, D.H., Rohl, A.L., 1995. Marvin—a new computer code for studying surfaces and interfaces and its application to calculating the crystal morphologies of corundum and zircon. *J. Chem. Soc. Faraday Trans.* **91**, 925–936.

Härtig, C., Brand, P., Bohmhammel, K., 1984. Fe–Al–Isomorphie and Strukturwasser in Kristallen vom Jarosit-Alunit-Typ. *Z. Anorg. Allg. Chem.* **508**, 159–164.

Hawthorne, F.C., Krivovichev, S.V., Burns, P.C., 2000. The crystal chemistry of sulphate minerals. In: Alpers, C.N., Jambor, J.L., Nordstrom, D.K. (Eds), *Sulfate Minerals: Crystallography, Geochemistry, and Environmental Significance*, Reviews in Mineralogy and Geochemistry 40, pp. 1–112.

Helgeson, H.C., 1969. Thermodynamics of hydrothermal systems at elevated temperatures and pressures. *Am. J. Sci.* **267**, 729–804.

Hendricks, S.B., 1937. The crystal structure of alunite and the jarosites. *Am. Miner.* **22**, 773–784.

Hudson-Edwards, K.A., Schell, C., Macklin, M.G., 1999. Mineralogy and geochemistry of alluvium contaminated by metal mining in the Rio Tinto area, southwest Spain. *Appl. Geochem.* **14**, 55–70.

Hyashi, H., 1994. Mineralogy and chemistry of jarosite and acid sulphate soils. *Nendo Kagaku* **34**, 118–124.

Jambor, J.L., 1999. Nomenclature of the alunite supergroup. *Can. Miner.* **37**, 1323–1341.

Jambor, J.L., Dutrizac, J.E., 1983. Beaverite-plumbojarosite solid solution. *Can. Miner.* **21**, 101–113.

Kubisz, J., 1964. A study of minerals in the alunite-jarosite group. *Polska Akad. Nauk. Prace Geol.* **22**, 1–93.

Kubisz, J., 1970. Studies on synthetic alkali-hydronium jarosites. I. Synthesis of jarosite and natrojarosite. *Miner. Pol.* **1**, 47–57.

Larson, A.C., Von Dreele, R.B., 1998. Computer-simulation studies of perfect and defective surfaces in Cr_2O_3. *J. Am. Ceramic Soc.* **71**, C389–C391.

Le Bail, A., Duroy, H., Fourquet, J.L., 1988. Abinitio structure determination of $LiSBWO_6$ by X-ray powder diffraction. *Materials Res. Bull.* **23**, 447–452.

Lewis, G.V., Catlow, C.R.A., 1985. Potential models for ionic oxides. *J. Phys. C-Solid State Phys.* **18**, 1149–1161.

McMillan, P.F., Hofmeister, A.M., 1988. Infrared and Raman spectroscopy. In: Hawthorne, F.C. (Ed.), *Spectroscopic Methods in Mineralogy and Geology*. Mineralogical Society of America.

Menchetti, S., Sabelli, C., 1976. Crystal chemistry of the alunite series; crystal structure refinement of alunite and synthetic jarosite. *Neues Jahrbuch fuer Mineralogie Monatshefte* **9**, 406–417.

Nordstrom, D.K., Munoz, J.L., 1994. *Geochemical Thermodynamics*, second ed. Blackwell Scientific Publications, Boston.

Powers, D.A., Rossman, G.R., Schugar, H.J., Gray, H.B., 1975. Magnetic behaviour and infrared spectra of jarosite, basic iron sulphate and their chromate analogs. *J. Sol. Stat. Chem.* **13**, 1–13.

Putnis, A., 2002. Mineral replacement reactions: from macroscopic observations to microscopic mechanisms. *Min. Mag.* **66**, 689–708.

Ripmeester, J., A, Ratcliffe, C.I., Dutrizac, J.E., Jambor, J.L., 1986. Hydronium in the alunite-jarosite group. *Can. Miner.* **22**, 773–784.

Sasaki, K., Konno, H., 2000. Morphology of jarosite-group compounds precipitated from biologically and chemically oxidized Fe ions. *Can. Mineral.* **38**, 45–56.

Sasaki, K., Ootuka, K., Watanabe, M., Tozawa, K., 1998. Solubility of sodium jarosite in sulphuric acid solution at temperature range of 70 to 110 °C. *Shigen-to-Sozai* **114**, 111–120.

Saul, P., Catlow, C.R.A., Kendrick, J., 1985. Theoretical-studies of protons in sodium-hydroxide. *Phil. Mag. B–Phys. Condensed Matter Statistical Mechanics Electronic Optical and Magnetic Properties* 51, pp. 107–117.

Schwertmann, U., 1961. The occurrence and origin of jarosite (maibolt) in marshy soil. *Naturwiss* **48**, 159–160.

Schwertmann, U., 1991. Solubility and dissolution of iron oxides. *Plant Soil* **130**, 1–25.

Serna, C.J., Cortina, C.P., Raymos, J.V.G., 1986. Infrared and Raman-study of alunite jarosite compounds. *Spectrachim. Acta* **42**, 729–734.

Stoffregen, R.E., 1993. Stability relations of jarosite and natrojarosite. *Geochim. Cosmochim. Acta* **57**, 2417–2419.

Stoffregen, R.E., Rye, R.O., 1992. Jarosite–water O-18 and D-fractionations. *Abstr. Pap. Am. Chem. Soc.* **204**, 86GEOC.

Stoffregen, R.E., Alpers, C.N., Jambor, J.L., 2000. Alunite–jarosite crystallography, thermodynamics and geochronology. *Rev. Miner. Geochem.* **40**, 453–479.

Stumm, W., Morgan, J.W., 1996. *Aquatic Chemistry*. Wiley-Interscience, New York.

Tasker, P.W., 1979. Stability of ionic crystal surfaces. *J. Chem. Phys. C: Solid State Phys.* **12**, 4977–4984.

World Health Organization 1996. *Guidelines for drinking-water quality. Second edition, Vol. 2 Health criteria and other supporting information*. WHO, Geneva., pp. 940–949.

World Health Organization 1998. *Guidelines for drinking-water quality. Second edition, Addendum to Vol. 2*. WHO, Geneva., pp. 281–283.

Wolery, T., 1979. Calculation of equilibrium between aqueous solution and minerals: the EQ3/6 software package. Lawrence Livermore National Laboratory, UCRL-52658.

Wolery, T., 1996. *EQ3/6 Database*. Lawrence Livermore National Laboratory, USA.

Woodley, S.M., Battle, P.D., Gale, J.D., Catlow, C.R.A., 1999. The prediction of inorganic crystal structures using a genetic algorithm and energy minimisation. *Phys. Chem. Chem. Phys.* **1**, 2535–2542.